A Numerical Study of Horizontal Roll Vortices in Neutral and Unstable Atmospheric Boundary Layers

Andreas Chlond

Max-Planck-Institut für Meteorologie, Hamburg

(Manuscript received 17.07.1986, in revised form 11.12.1986)

Abstract:

The non-linear dynamics of horizontal roll vortices in neutral and unstable atmospheric boundary layers are investigated by means of a numerical spectral model. The large-scale eddies are assumed to be two-dimensional and they are modelled explicitly in a vertical plane with variable orientation with respect to the geostrophic wind.

First, the linear stability of the system is discussed for various Richardson numbers to confirm that the fundamental instability mechanisms leading to the occurence of rolls are the inflection point instability and shear organized buoyant convection. In addition, finite amplitude integrations are performed. From this, it is found that the perturbations come to a non-linear equilibrium, producing a modified mean flow and a helical roll secondary circulation with a horizontal wavelength of about three times the convection layer depth.

Emphasis is placed on the roll kinetic energy budget to evaluate the importance of the various energy exchange processes in the production and maintenance of rolls. The model results indicate that the rolls in an atmospheric boundary layer with thermally unstable stratification are maintained primary by buoyancy and secondary by production of energy from the cross-roll component of the mean wind spiral (inflection point instability).

Finally, the calculated roll parameters such as aspect ratio and orientation angle as well as the calculated profiles of roll-scale velocity variances, transports of temperature, along- and cross-roll momentum are compared with measurements.

Zusammenfassung: Eine numerische Studie von Wirbelrollen in neutralen und instabil geschichteten atmosphärischen Grenzschichten

Die nichtlineare Dynamik von Rollen wird mit Hilfe eines numerischen spektralen Modells in neutralen und instabilen atmosphärischen Grenzschichten untersucht.

Bei der Beschreibung rollenartiger Bewegungen wird von der zweidimensionalen Näherung Gebrauch gemacht, so daß die Rollen explizit in einer Ebene, die hinsichtlich der Richtung des geostrophischen Windes eine beliebige Orientierung aufweisen kann, modelliert werden können.

Zunächst wird mit Hilfe einer linearisierten Version des Modells gezeigt, daß die Bildung von Wirbeln mit horizontaler Rotationsachse zum einen durch die Wendepunktsinstabilität und zum anderen bei labiler Dichteschichtung durch die thermische Instabilität ausgelöst werden kann.

Außerdem wurden Integrationen der nichtlinearen Gleichungen durchgeführt. Die Rechnungen zeigen, daß sich Zellstrukturen mit einem Aspektverhältnis von ca. drei entwickeln, die durch Rückkoppelungsprozesse die instabilen Grundstromprofile so verändern, daß sie in Verbindung mit der Sekundärzirkulation eine stabile Konfiguration darstellen. Bei den Berechnungen wird ein besonderes Augenmerk auf die Energetik der Rollen geworfen, die direkte Einblicke in die Instabilitätsmechanismen ermöglicht. Es kann gezeigt werden, daß bei labiler Dichteschichtung die Rollen primär durch die durch Auftrieb produzierte Energie und sekundär durch die durch Scherung produzierte Energie gespeist werden.

Schließlich werden die berechneten Rollenparameter, wie Aspektverhältnis und Orientierungswinkel, sowie die berechneten Höhenprofile der Geschwindigkeitsvarianzen, der Transporte von Temperatur, lateralem und longitudinalem Impuls in der Rollenskala mit Meßdaten verglichen.

0005-8173/87/02 0144–26 $ 03.00/0

Résumé: Une étude numérique de tourbillons horizontaux dans des couches limites atmosphériques neutres et instables

On étudie la dynamique non linéaire de tourbillons horizontaux dans des couches limites atmosphériques neutres et instables à l'aide d'un modèle numérique spectral. Les perturbations de grande échelle sont supposées être à deux dimensions et sont modélisées explicitement dans un plan vertical d'orientation variable par rapport au vent géostrophique.

On discute d'abord la stabilité linéaire du système pour divers nombres de Richardson afin de confirmer que les mécanismes fondamentaux d'instabilité conduisant à l'apparition de rouleaux sont l'instabilité de point d'inflexion et la convection de flottabilité organisée par le cisaillement. De plus, des intégrations avec amplitudes finies sont réalisées. On trouve alors que les perturbations attaignent un équilibre non linéaire engendrant un écoulement moyen modifié et une circulation secondaire constituée d'un tourbillon hélicoidal dont la longueur d'onde horizontale vaut environ trois fois la profondeur de la couche convective. Afin d'évaluer l'importance des divers processus d'échange d'énergie dans la production et le maintien des rouleaux, on s'intéresse particulièrement au bilan de leur énergie cinétique. Les résultats du modèle indiquent que lorsque la stratification thermique est instable, les rouleaux sont maintenus en premier lieu par la flottabilité et en deuxième lieu, par la production d'énergie à partir de la composante du vent moyen transversalement aux rouleaux (instabilité de point d'inflexion).

Finalement, les paramètres calculés des rouleaux comme le rapport de forme et l'angle d'orientation de même que les profils des variances du champ de vitesse à l'échelle des rouleaux, des transports de température, de la quantité de mouvement le long et transversalement aux rouleaux sont comparés avec les mesures.

1 Introduction

Satellite imagery of the Earth's surface has revealed the frequent occurrence of large areas of organized linear cloud patterns, particularly over the oceans. These areas are usually associated with the flow of cold air over warm water such as in cold air outbreaks in mid-latitudes. Since these organized convective motions transport and redistribute momentum energy and matter it seems reasonable to suppose that there are substantial feedback effects between these motions and the larger scale mean flow. It is consequently of interest to study these phenomena in order to understand the mechanisms inherent to them and to estimate their importance in large scale atmospheric processes.

Observations of KÜTTNER (1971) clearly show the character of these circulations. When the wind is sufficiently high and the heat flux not too strong the data show that the convective patterns exhibit nearly a two-dimensional structure. The conception is that these meso-scale eddies consist of almost longitudinal vortex rolls which extend throughout the depth of the boundary layer, bounded by an inversion layer above. They are superimposed upon and interact with both the basic boundary layer flow and a fine grained turbulence field, yet are capable of retaining their characteristic form. Their axis is almost in the direction of the basic flow and parallel stripes of upward motion within these helical motions may be marked with clouds. The spacing between adjacent cloud lines is normally between 2 and 8 km and the lines can be up to 500 km length.

The formation of longitudinal vortex rolls in fluid layers has been subjected to numerous experimental and theoretical studies. These studies suggest that cloud streets occur as a result of a combination of two dynamic and one thermodynamic mechanism, commonly labeled the inflection point, the parallel, and the Rayleigh-Bénard instability. Realistic roll wavelength- to height ratios and orientations to the geostrophic wind are reproduced by linear models based on inflectional instability (e.g., those of LILLY, 1966; ETLING and WIPPERMANN, 1975) or buoyancy combined with shear (e.g. BROWN, 1972; ASAI, 1973; WIPPERMANN et. al., 1978).

However, the linear theory is only valid at the onset of convection when the non-linear advection terms in the governing equations are small. The principal merit of the non-linear solution is the possibility of

investigation of finite amplitude steady state disturbances and determination of transports of momentum and energy provided by the rolls. A finite amplitude study of boundary layer rolls in an asymptotic boundary layer has been performed by BROWN (1970). He assumed that the finite perturbations preserve the structure of the infinitesimal perturbations for the dynamic instability of the Ekman boundary layer. In addition, he hypothesized that the helical roll secondary circulations come to an equilibrium. To establish this equilibrium, an energetic criterion, zero net energy transfer from the mean flow to the perturbations, was employed. BROWN (1970) computed-finite amplitude equilibrium roll magnitudes over a wide range of the external parameters and found that these finite disturbances alter the mean velocity profile such that it becomes stable.

MASON and SYKES (1982) numerically integrated the Boussinesq equations in finite difference form and found that in the convective case of an unstable boundary layer the thermal instability mode to be dominant with an orientation of the vortex rolls in agreement with the observations. In addition, their study has provided a better understanding of the physical processes involved, and has given a detailed information on roll-scale velocity variances and roll-scale vertical transports.

Although observations and satellite pictures indicate that there are three-dimensional elements within the quasi-two-dimensional roll organization, nearly all linear and non-linear studies on the boundary layer roll problem have assumed homogeneous conditions in the direction of the roll axis. BECKER (1987) discarded this asumption. His model allows the energy containing eddies to be modelled in three dimensions, along with the imposition of a lid at a higher level above the boundary layer. A key result was that the resolved structure resembles that of thermal instability theory and that the model is capable to give the relation between longitudinal and lateral velocity variance in a right manner.

Other investigators have studied low-order spectral models of thermal and dynamic convection (e.g. SHIRER, 1980; CHLOND, 1985) in order to gain more insight into some of the non-linear aspects of convection in the atmospheric boundary layer. However, due to the severe truncation they use to represent the convective solutions it cannot be expected that these models describe the developing structures in detail.

LE MONE (1973) has done a very thorough observational analysis of the rolls, using aircraft and tower data. Their observations have provided a better understanding of the instability mechanisms operating in the atmosphere and have allowed to determine structure and related statistics of energy containing eddies within the atmospheric boundary layer. In addition, she compared observed roll magnitudes to those obtained for BROWNs (1970) finite-amplitude equilibrium inflectional instability rolls. She inferred that the rolls had a shape well determined by shear theory but with amplitudes systematically to low. LE MONE (1973) concluded that some additional surface heating is needed in order to provide larger equilibrium secondary flow magnitudes. BRÜMMER (1985) also presented aircraft measurements made in the presence of boundary layer rolls and was able to analyse the roll strucutre and to determine some of the generation terms in the roll kinetic energy budget. He reported on three cases of boundary layer roll observations for which it has been possible to quantify the processes leading to the formation of rolls. His observations so far indicate that dynamic and convective instability usually dominate roll development, but the relative importance of these two mechanisms varies from case to case and still has to be investigated in more detail.

In the present study, the objective is to investigate the non-linear dynamics of horizontal roll vortices in an inversion capped boundary layer generated by the combined effect of inflection point instability and instability due to heating from below. The large scale eddies are assumed to be two-dimensional and they are modelled explicitly in a vertical plane of variable orientation with respect to the geostrophic wind. In contrast to the models of MASON and SYKES (1982) and BECKER (1987) which use the grid point method we apply the spectral method to solve the partial differential equations because the spectral method is much more accurate (MACHENHAUER, 1979). In the grid point method the major source of

truncation error is distortion of space derivatives through approximation with finite differences resulting in pseudo-diffusion of momentum and heat. In addition, another advantage of the spectral method is to trace in which way energy and momentum are interchanged between convective elements of different horizontal sizes. Therefore, emphasis is placed on the spectral roll kinetic energy budget to evaluate the importance of the various energy exchange processes in the production and maintenance of rolls. The aim of the work is therefore to understand how the properties and dynamics of such rolls depend upon the relative importance of shear and buoyant forces.

In Section 2 the basic equations and numerical techniques are outlined. The subsequent Sections will report on the information which the model yields concerning the linear stability of the system and the properties of the full non-linear integrations. In addition, a comparison of the model results with measurements is performed to demonstrate possibilities and limitations of two-dimensional modelling.

2 Model

2.1 Governing equations

To develop the model we consider here shallow Boussinesq-convection arising in a rotating fluid that is forced both thermally and dynamically. The analysis is carried out in a coordinate system whose x-axis is orientated along the roll axis and is turned by an angle λ against the geographic east direction (see Figure 1). In addition, the vortices are assumed to be two-dimensional, i.e. there are no variations in the x-direction except for a background pressure gradient which, together with its y-component, provides a geostrophic flow making an angle $-\epsilon$ with the x-axis.

For convenience of numerical analysis we divide the velocity- and temperature fields into two parts, a barotropic horizontal homogenous mean state, denoted by an overbar, and a finite amplitude perturbation, denoted by a prime. Hence, the velocity and state variables can be written as

$$\underline{v}(y, z, t) = \bar{\underline{v}}(z, t) + \underline{v}'(y, z, t) \tag{1}$$

$$T(y, z, t) = \bar{T}(z, t) + T'(y, z, t) \, . \tag{2}$$

Because $\partial v'/\partial y + \partial w'/\partial z = 0$ in the Boussinesq-system we introduce a stream function ψ with the definition

$$v' = -\frac{\partial \psi}{\partial z} \qquad w' = \frac{\partial \psi}{\partial y} \, . \tag{3}$$

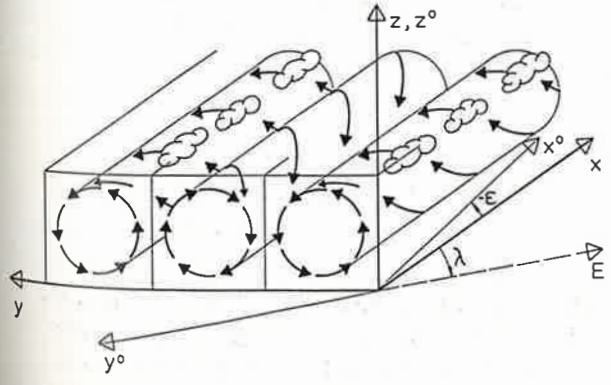

• **Figure 1**
Illustrating the coordinate system used for numerical integrations.

The two-dimensional convection equations are now expressed in terms of two sets of differential equations. One is for momentum and temperature of the horizontal homogeneous base state. The second is for the perturbations of the longitudinal wind component, the temperature, and the vorticity of the motions normal to the x-axis. With the definitions of the vorticity $\nabla^2 \psi$ and the Jacobian operator J,

$$\nabla^2 \psi = \frac{\partial w'}{\partial y} - \frac{\partial v'}{\partial z}$$

$$J(a, b) = \frac{\partial a}{\partial y}\frac{\partial b}{\partial z} - \frac{\partial a}{\partial z}\frac{\partial b}{\partial y} \tag{4}$$

we have

$$\frac{\partial \bar{u}}{\partial t} = f_1(\bar{v} + |\underline{v}_g| \sin\epsilon) + \frac{\partial}{\partial z}\left(K_M \frac{\partial \bar{u}}{\partial z}\right) - \frac{\partial}{\partial z}(\overline{u'w'}) \tag{5}$$

$$\frac{\partial \bar{v}}{\partial t} = -f_1(\bar{u} - |\underline{v}_g| \cos\epsilon) + \frac{\partial}{\partial z}\left(K_M \frac{\partial \bar{v}}{\partial z}\right) - \frac{\partial}{\partial z}(\overline{v'w'}) \tag{6}$$

$$\frac{\partial \bar{T}}{\partial t} = -\nabla \underline{F}_R + \frac{\partial}{\partial z}\left(K_T \frac{\partial \bar{T}}{\partial z}\right) - \frac{\partial}{\partial z}(\overline{w'T'}) \tag{7}$$

$$\frac{\partial u'}{\partial t} = -\bar{v}\frac{\partial u'}{\partial y} - \frac{\partial \psi}{\partial y}\frac{\partial \bar{u}}{\partial z} - J(\psi, u') + J(\overline{\psi, u'}) - f_1 \frac{\partial \psi}{\partial z} - f_2 \frac{\partial \psi}{\partial y}\cos\lambda + K_M \frac{\partial^2 u'}{\partial y^2} + \frac{\partial}{\partial z}\left(K_M \frac{\partial u'}{\partial z}\right) \tag{8}$$

$$\frac{\partial T'}{\partial t} = -\bar{v}\frac{\partial T'}{\partial y} - \frac{\partial \psi}{\partial y}\frac{\partial \bar{T}}{\partial z} - J(\psi_1, T') + J(\overline{\psi, T'}) + K_T \frac{\partial^2 T'}{\partial y^2} + \frac{\partial}{\partial z}\left(K_T \frac{\partial T'}{\partial z}\right) \tag{9}$$

$$\frac{\partial}{\partial t}(\nabla^2 \psi) = -\bar{v}\frac{\partial}{\partial y}(\nabla^2 \psi) + \frac{\partial \psi}{\partial y}\frac{\partial^2 \bar{v}}{\partial z^2} - J(\psi, \nabla^2 \psi) + J(\overline{\psi, \nabla^2 \psi}) + f_1 \frac{\partial u'}{\partial z} + f_2 \frac{\partial u'}{\partial y}\cos\lambda + \frac{g}{T_0}\frac{\partial T'}{\partial y} + K_M \nabla^2(\nabla^2 \psi) + 2\frac{\partial K_M}{\partial z}\frac{\partial}{\partial z}(\nabla^2 \psi) + \frac{\partial^2 K_M}{\partial z^2}\frac{\partial^2 \psi}{\partial z^2}. \tag{10}$$

The overbars indicate the horizontal average over an area equal in size to that treated; $|\underline{v}_g|$ denotes the modulus of the geostrophic wind, assumed to be constant in space and time; $\nabla \underline{F}_R$ is a rate of temperature change associated with the divergence of radiative flux; f_1 and f_2 are the vertical and the horizontal component of the Coriolis parameter, respectively; and K_M and K_T are taken to be eddy values of viscosity and thermometric conductivity.

2.2 Region treated and boundary conditions

The domain extended to a height of $z = z_I$ where a lid was imposed in crude simulation of an inversion base, assuming that its height is known from observations. Furthermore, we introduce into the problem a surface layer, whose depth z_P we assume to be given.

We consider neutral and unstable atmospheric boundary layers and suppose that the rolls develop only in the layer between the surface layer and the inversion layer in which the flow field is determined by the Equations (5)–(10). In the surface layer between $z_0 \leqslant z \leqslant z_P$ the similarity hypothesis of Monin

and Obukhov has been used as a basis for the description of mean wind speed and temperature. Therefore, we obtain the relations

$$\bar{u}(z) = \kappa^{-1}\, u_* \cos\alpha \,\{\ln(z/z_0) - \psi_M(z/L)\} \tag{11}$$

$$\bar{v}(z) = \kappa^{-1}\, u_* \sin\alpha \,\{\ln(z/z_0) - \psi_M(z/L)\} \qquad z_0 \leqslant z \leqslant z_P \tag{12}$$

$$\bar{T}(z) = \kappa^{-1}\, T_* \,\{\ln(z/z_0) - \psi_H(z/L)\} \tag{13}$$

where κ is the von Kármán constant, z_0 the roughness length, α is the angle between the surface stress and the x-axis of the coordinate system and the scaling velocity and temperature are defined from the vertical turbulent eddy fluxes of momentum $\overline{u'w'}$ and sensible heat $\overline{w'T'}$

$$\alpha = \arctan\{\bar{v}(z_P)/\bar{u}(z_P)\} \tag{14}$$

$$u_* = \{|\overline{u'w'}|\}^{1/2} = \frac{\kappa\,\{\bar{u}^2(z_P) + \bar{v}^2(z_P)\}^{1/2}}{\{\ln(z_P/z_0) - \psi_M(z_P/L)\}} \tag{15}$$

$$T_* = -(\overline{w'T'})/u_* = \frac{\kappa\,\{\bar{T}(z_P) - \bar{T}(z_0)\}}{\{\ln(z_P/z_0) - \psi_H(z_P/L)\}}$$

L is the Monin-Obukhov scale height

$$L = \frac{u_*^2}{\kappa\,(g/T_0)\,T_*}$$

where g is the acceleration due to gravity. The functions ψ_M and ψ_H are defined by

$$\psi_M(z/L) = \int_{z_0}^{z} \frac{1 - \Phi_M(z/L)}{z}\,dz \tag{17}$$

$$\psi_H(z/L) = \int_{z_0}^{z} \frac{1 - \Phi_H(z/L)}{z}\,dz \tag{18}$$

where Φ_M and Φ_H are non-dimensional shear functions for momentum and sensible heat respectively. In this study, we assume the following empirical relations with reference to BUSINGER (1971) for these functions

$$\Phi_M(z/L) = \{1 - 16(z/L)\}^{-1/4} \qquad z/L < 0 \tag{19}$$

$$\Phi_H(z/L) = 0.74\,\{1 - 9(z/L)\}^{-1/2} \tag{20}$$

For the eddy diffusivities K_M and K_T in the lowest shallow layer between z_0 and z_P we assume the following relations

$$K_M = \frac{\kappa\, u_*\, z}{\Phi_M(z/L)} \tag{21}$$

$$K_T = \frac{\kappa\, u_*\, z}{\Phi_H(z/L)} \qquad z_0 \leqslant z \leqslant z_P \tag{22}$$

Values of K_M and K_T above the surface layer are given by an interpolation formula

$$K_{(M,T)} = \begin{cases} K_{(M,T)}\,(z = z_P) + \gamma_1 (z - z_P) & z_P \leqslant z \leqslant z_M \\ K_{(M,T)}\,(z = z_M)\exp(-\gamma_2\,(z - z_M)) & z_M \leqslant z \leqslant z_I \end{cases} \tag{23}$$

which yields a profile with a linear increase of $K_{(M,T)}$ from the top of the surface layer to some level at $z = z_M$ within the atmospheric boundary and then an exponential decrease with height. The constants γ_1 and γ_2 could be determined by specifying values of $K_{(M,T)}$ at the level $z = z_M$ and at the inversion base In the present study it is assumed that the maximum of $K_{(M,T)}$ lies $0.4(z_I - z_P)$ above the top of the surface layer where the diffusion coefficients are 5.5 times larger than at the top of the surface layer. At the inversion base a small near zero value for $K_{(M,T)}$ is specified (5% of $K_{(M,T)}(z_P)$).

The boundary conditions for the perturbation Equations (8)–(10) are based on the assumptions that the boundaries $z = z_P$, $z = z_I$, are perfect conductors of heat and are flat and stress free. Then the conditions are

$$\frac{\partial u'}{\partial z} = \psi = \nabla^2 \psi = T' = 0 \,, \qquad \text{on } z = z_P, z_I \tag{25}$$

In the cross-stream (y)-direction the width of the model domain was $L = 9.6(z_I - z_P)$ in the neutral case and $5.6(z_I - z_P)$ in the unstable cases. At the vertical sides of the volume treated, cyclic boundary conditions are imposed upon u', ψ and T'.

With respect to the mean flow we require geostrophic and adiabatic conditions at the upper boarder, respectively.

$$\bar{u} = |\underline{v}_g| \cos\epsilon \qquad \bar{v} = -|\underline{v}_g| \sin\epsilon \qquad \frac{d\bar{T}}{dz} = 0 \qquad \text{on } z = z_I \tag{25}$$

At $z = z_P$ the conditions

$$\begin{aligned} \frac{d\bar{u}}{dz} &= \frac{u_* \cos\alpha}{\kappa z_P} \Phi_M(z_P/L) \\ \frac{d\bar{v}}{dz} &= \frac{u_* \sin\alpha}{\kappa z_P} \Phi_M(z_P/L) \qquad \text{on } z = z_P \\ \frac{d\bar{T}}{dz} &= \frac{T_*}{\kappa z_P} \Phi_H(z_P/L) \end{aligned} \tag{26}$$

were specified, providing the continuity of $\bar{u}$, $\bar{v}$, $\bar{T}$, $\partial\bar{u}/\partial z$, $\partial\bar{v}/\partial z$ and $\partial\bar{T}/\partial z$ at $z = z_P$

2.3 Non-dimensional forms

We will cast the equations in non-dimensional form by using $(z_I - z_P)$, $|\underline{v}_g|$, $(\bar{T}(z_P) - \bar{T}(z_0))$ and $K_M(z_P)$ as scale factors for length, velocity, temperature and diffusivity. The non-dimensional variables are denoted by the symbol "^" as follows

$$\begin{aligned} &y = (z_I - z_P)\hat{y}, \qquad z = z_P + (z_I - z_P)\hat{z}, \qquad t = \hat{t}(z_I - z_P)/|\underline{v}_g| \\ &(\bar{u}, \bar{v}) = (\hat{\bar{u}}, \hat{\bar{v}})|\underline{v}_g|, \qquad (u', v', w') = (\hat{u}', \hat{v}', \hat{w}')|\underline{v}_g|, \qquad \psi = \hat{\psi}\,|\underline{v}_g|\,(z_I - z_P) \\ &\bar{T} = \bar{T}(z_0) + (\bar{T}(z_P) - \bar{T}(z_0))\hat{\bar{T}}, \qquad T' = (\bar{T}(z_P) - \bar{T}(z_0))\hat{T}' \\ &K_{(M,T)} = K_M(z_P)\hat{K}_{(M,T)} \end{aligned}$$

Introducing these transformations into Equations (5)–(10) and dropping hats leads to

$$\frac{\partial\bar{u}}{\partial t} = \mathrm{Ro}^{-1}(\bar{v} + \sin\epsilon) + \mathrm{Re}^{-1}\frac{\partial}{\partial z}\left(K_M \frac{\partial\bar{u}}{\partial z}\right) - \frac{\partial}{\partial z}(\overline{u'w'}) \tag{27}$$

$$\frac{\partial\bar{v}}{\partial t} = -\mathrm{Ro}^{-1}(\bar{u} - \cos\epsilon) + \mathrm{Re}^{-1}\frac{\partial}{\partial z}\left(K_M \frac{\partial\bar{v}}{\partial z}\right) - \frac{\partial}{\partial z}(\overline{v'w'}) \tag{28}$$

$$\frac{\partial \bar{T}}{\partial t} = -\frac{(z_I - z_P)}{|\underline{v}_g|(\bar{T}(z_P) - \bar{T}(z_0))}\left(\nabla \underline{F}_R + \frac{\partial \bar{T}(z_0)}{\partial t}\right) + Re^{-1} Pr^{-1} \frac{\partial}{\partial z}\left(K_T \frac{\partial \bar{T}}{\partial z}\right) - \frac{\partial}{\partial z}(\overline{w'T'}) \quad (29)^*$$

$$\frac{\partial u'}{\partial t} = -\bar{v}\frac{\partial u'}{\partial y} - \frac{\partial \psi}{\partial y}\frac{\partial \bar{u}}{\partial z} - J(\psi, u') + J(\overline{\psi, u'}) - Ro^{-1}\frac{\partial \psi}{\partial z} - Ro^{*-1}\frac{\partial \psi}{\partial y} +$$

$$+ Re^{-1}\left\{K_M \frac{\partial^2 u'}{\partial y^2} + \frac{\partial}{\partial z}\left(K_M \frac{\partial u'}{\partial z}\right)\right\} \quad (30)$$

$$\frac{\partial T'}{\partial t} = -\bar{v}\frac{\partial T'}{\partial y} - \frac{\partial \psi}{\partial y}\frac{\partial \bar{T}}{\partial z} - J(\psi, T') + J(\overline{\psi, T'}) + Pr^{-1} Re^{-1}\left\{K_T \frac{\partial^2 T'}{\partial y^2} + \frac{\partial}{\partial z}\left(K_T \frac{\partial \bar{T}'}{\partial z}\right)\right\} \quad (31)$$

$$\frac{\partial}{\partial t}(\nabla^2 \psi) = -\bar{v}\frac{\partial}{\partial y}(\nabla^2 \psi) + \frac{\partial \psi}{\partial y}\frac{\partial^2 \bar{v}}{\partial z^2} - J(\psi, \nabla^2 \psi) + J(\overline{\psi, \nabla^2 \psi}) + Ro^{-1}\frac{\partial u'}{\partial z} + Ro^{*-1}\frac{\partial u'}{\partial y} +$$

$$+ Ri\frac{\partial T'}{\partial y} + Re^{-1}\left\{K_M \nabla^2(\nabla^2 \psi) + 2\frac{\partial K_M}{\partial z}\frac{\partial}{\partial z}(\nabla^2 \psi) + \frac{\partial^2 K_M}{\partial z^2}\frac{\partial^2 \psi}{\partial z^2}\right\} \quad (32)$$

where,

$Ro = \dfrac{|\underline{v}_g|}{f_1(z_I - z_P)}$ $\quad Ro^* = \dfrac{|\underline{v}_g|}{f_2(z_I - z_P)\cos\lambda}$, the Rossby numbers;

$Re = \dfrac{|\underline{v}_g|(z_I - z_P)}{K_M(z_P)}$, the Reynolds number;

$Pr = \dfrac{K_M(z_P)}{K_T(z_P)}$, the Prandtl number;

$Ri = \dfrac{(g/T_0)(\bar{T}(z_P) - \bar{T}(z_0))/(z_I - z_P)}{|\underline{v}_g|^2/(z_I - z_P)^2}$, the Richardson number.

The corresponding boundary conditions are

$$\frac{\partial u'}{\partial z} = \psi = \nabla^2 \psi = T' = 0 \quad \text{on } z = 0,1 \quad (33)$$

$$\frac{d\bar{u}}{dz} = \frac{(z_I - z_P)}{z_P}\frac{u_*}{\kappa}\cos\alpha\,\Phi_M(z_P/L)$$

$$\frac{d\bar{v}}{dz} = \frac{(z_I - z_P)}{z_P}\frac{u_*}{\kappa}\sin\alpha\,\Phi_M(z_P/L) \quad \text{on } z = 0 \quad (34)$$

$$\frac{d\bar{T}}{dz} = \frac{(z_I - z_P)}{z_P}\frac{T_*}{\kappa}\Phi_H(z_P/L)$$

$$\bar{u} = \cos\epsilon \qquad \bar{v} = -\sin\epsilon \qquad \frac{d\bar{T}}{dz} = 0 \quad \text{on } z = 1 \quad (35)$$

The non-dimensional parameters Ro, Ro*, Pr, Ri, Re, $(z_I - z_P)/z_P$, z_P/L and $\ln(z_P/z_0)$ appearing in Equations (27)–(35) are not independent from each other. In particular, Re and Pr cannot be treated as variable parameters since the eddy diffusivities included in these quantities are not a property of the fluid but depend upon the flow conditions. Therefore, Re, Pr as well as z_P/L are itself a part of the results of the calculations and could be determined as functions of the other parameters. Hence, the non-dimensional parameters to be varied independently are Ro, Ro*, $(z_I - z_P)/z_P$, $\ln(z_P/z_0)$ and Ri.

In Equation (29)* the divergence of the radiative flux and the rate at which the surface value of $\overline{T}(z_0)$ increases with time have to be specified. Since heat, in general, is continually being fed into the air from the surface in this problem and none leaves the level z = 1, the temperature $\overline{T}$ itself cannot attain an equilibrium profile. However, $\hat{\overline{T}}$ depends upon $\overline{T} - \overline{T}(z_0)$, so that $\hat{\overline{T}}$ can indeed achieve a steady state. This requires the first term in Equation (29)* to balance the vertical divergence of the turbulent and convective heat flux. The condition for this balance, from Equation (29)*, is

$$-\frac{(z_I - z_P)}{|\underline{v}_g|(\overline{T}(z_P) - \overline{T}(z_0))}\left\{\nabla \underline{F}_R + \frac{\partial \overline{T}(z_0)}{\partial t}\right\} = -\frac{\partial}{\partial z}\left(Pr^{-1} Re^{-1} K_T \frac{\partial \overline{T}}{\partial z} - \overline{w'T'}\right) = \frac{\partial}{\partial z} H_{TOT} \qquad (36)$$

From Equation (36), we see that either the terms on the left hand side could be individually specified, or, equivalently the total heat flux H_{TOT} could be specified. The latter procedure was employed so that realistic temperature and heat flux profiles would be achieved. The assumed profile of the total heat flux is defined by use of a forcing function T_F

$$-H_{TOT} = Pr^{-1} Re^{-1} K_T \frac{dT_F}{dz}$$

Equation (29)* then becomes

$$\frac{\partial \overline{T}}{\partial t} = Pr^{-1} Re^{-1} \frac{\partial}{\partial z}\left\{K_T \frac{\partial}{\partial z}(\overline{T} - T_F)\right\} - \frac{\partial}{\partial z}(\overline{w'T'}) \qquad (29)$$

The profile assumed for T_F is designed in a manner so that vertical gradients of the mean temperature $\overline{T}$ are confined to the lower third of the atmospheric boundary layer.

$$T_F = 1 + \frac{T_*}{\kappa} \frac{(z_I - z_P)}{z_P} \Phi_H(z_P/L) \frac{1}{6.9}\{1 - \exp(-6.9\, z)\}$$

2.4 Method of solution

The equations for the mean flow quantities (27)–(29) are replaced by finite difference approximations using (N − 1) constant intervals of width $\Delta z = 1/(N-1)$ in the vertical direction. The variables $\bar{u}$, $\bar{v}$, and $\overline{T}$ are defined at discrete intervals of z, i.e. $z = 0, \Delta z, 2\Delta z, \ldots, (N-1)\Delta z$ and the derivatives of these variables are replaced by centered differences. There are N = 11 mesh points in the vertical direction for all cases investigated.

In contrast, the perturbation Equations (30)–(32) are solved using spectral methods. In accord with the remarks in the introduction we assume that the evolved secondary motion field after instability has the form of two-dimensional rolls, independent of the x-direction and with a basic horizontal wavenumber denoted by $2\pi/L/H$ which will be specified later. Then a general spatial representation which satisfies the boundary conditions is

$$u'(y,z,t) = \sum_{n=-P}^{P} \sum_{m=0}^{M} u_{n,m}(t) \exp\left(i \cdot n \frac{2\pi}{L/H}\right) \cos(m \cdot \pi \cdot z)$$

$$\psi(y,z,t) = \sum_{n=-P}^{P} \sum_{m=1}^{M} \psi_{n,m}(t) \exp\left(i \cdot n \frac{2\pi}{L/H}\right) \sin(m \cdot \pi \cdot z) \qquad (37)$$

$$T'(y,z,t) = \sum_{n=-P}^{P} \sum_{m=1}^{M} T_{n,m}(t) \exp\left(i \cdot n \frac{2\pi}{L/H}\right) \sin(m \cdot \pi \cdot z)$$

where the $u_{n,m}$, $\psi_{n,m}$ and $T_{n,m}$ are generally functions of time. In our treatment we shall truncate the representations by choosing finite values of P and M. In the present study the truncated system consists of the components included by the components $n \leqslant P = 8$ and $m \leqslant M = 7$. The set of $2P(3M+1)$ ordinary differential equations governing the time variations of the amplitudes of the harmonic components is obtained via Fourier-transformation of Equations (30)–(32).

These are in symbolic form

$$\frac{d}{dt} e_i^{(n)} = \sum_j (\tilde{\Omega}_{ij}^{(n)} + \hat{\Omega}_{ij}^{(n)}) e_j^{(n)} + \sum_{o,p} \sum_{l,k} D_{n,o,p}^{i,l,k} e_i^{(o)} e_k^{(p)} \tag{38}$$

where $e_i^{(n)}$ denotes a vector gathering up all Fourier-components of the motion and temperature fields with the horizontal wavenumber n.

$$\underline{e}^{(n)} = (u_{n,o}, u_{n,1}, \ldots, u_{n,M}, \psi_{n,1}, \ldots, \psi_{n,M}, T_{n,1}, \ldots, T_{n,M})$$

The non-linear interactions of each wave with the mean flow are represented by the terms $\Sigma \tilde{\Omega}_{ij}^{(n)} e_j^{(n)}$. Convolution integrals which appear in the matrix $\tilde{\Omega}_{ij}^{(n)}$ like e.g.

$$\int_0^1 \bar{v} \sin(i \cdot \pi \cdot z) \sin(j \cdot \pi \cdot z) dz$$

are calculated at each time step using Simpson's rule. Effects of rotation, buoyancy production and of viscous damping are included in the terms $\Sigma \hat{\Omega}_{ij}^{(n)} e_j^{(n)}$. Finally, the quadratic terms represent non-linear interactions among the waves.

For time integration of Equation (38) and of the finite-difference form of Equations (27)–(29), the Runge-Kutta explicit scheme was choosen. The time step usually employed had a dimensionless magnitude of $\Delta t = 1$. Each time step required 6s CPU time for CDC 830 computer.

3 Results

3.1 Parameters considered and initial conditions

This paper concentrates on results obtained with parameters typical of those under which large scale rolls are seen in atmospheric observations. In the present study the following values for the non-dimensional parameters are used

$$\frac{(z_I - z_P)}{z_P} = 23 \qquad \ln\left(\frac{z_P}{z_0}\right) = 11 \qquad Ro^{-1} = 7.2 \cdot 10^{-3} \qquad Ro^{*-1} = 0$$

The parameters used are based on observations of the mean kinematic state of the atmosphere during the period 12.00–14.00 GMT on the 20th September 1981 in the KonTur experiment. During this period destinct cloud streets aligned nearly parallel to the mean wind direction were observed with a horizontal wavelength of about three times the convection layer depth. The geostrophic wind speed was about $|v_g| = 20$m/s and the depth of the roll layer was estimated to be 1200m thick (see BRÜMMER, 1985). Therefore, with a Coriolis parameter of $f_1 = 1.2 \cdot 10^{-4} s^{-1}$, a roughness length of $z_0 = 8.35 \cdot 10^{-4}$m and a surface layer depth of $z_P = 50$m a detailed comparison between results obtained from the model and measurements performed during this day is possible.

In particular, we are seeking to see to what extend the model is capable of reproducing organized cloud bands and is able to give quantitative results concerning the nature of heat and momentum fluxes. Since

the cloudy part of the roll circulation was observed to be rather small we assume that the release of latent heat due to condensation was not essential to the formation of convective streets. Therefore, a test of the model results against the observational data may be justified.

In order to understand how the structure and dynamics of such rolls depend upon the relative importance of shear and buoyant forces a series of numerical integrations for values of the Richardson number equal to

$$\mathrm{Ri} = (0.,\ -0.05,\ -0.10,\ -0.15)$$

have been conducted. Results of these integrations are presented and discussed in subsequent sections. With $|\underline{v}_g| = 20\,\mathrm{m/s}$, $(z_I - z_P) = 1150\,\mathrm{m}$, and a buoyancy parameter of $g/T_0 = 3.4 \cdot 10^{-2}\,\mathrm{m/(s^2 K)}$ these Richardson numbers correspond to temperature differences between the top and the bottom of the surface layer of about 0 K, −0.5 K, −1 K, and −1,5 K, respectively.

The initial condition for the integration is the steady state, horizontal homogeneous boundary layer solution, obtained by solving Equations (27)–(29) in which the divergence terms are neglected. In order to drive the system this initial, steady state, one-dimensional solution is then perturbed by imposing small perturbations on the complex Fourier-coefficients $e_i^{(n)}$ at the first time step.

In addition, results of a perturbation analysis were used as a basis for selecting the length of the horizontal domain and the angle ϵ of the domain relative to the geostrophic wind. The orientation angle and the length treated in the cross-stream direction are choosen so as to include four wavelengths of the most unstable linear mode.

3.2 Results of perturbation analysis

The first objective of this work was to examine the stability of the homogeneous, steady state boundary layer solution with respect to infinitesimal disturbances.

The relevant equation governing small amplitude perturbation motions is Equation (38) in which quadratic terms are neglected. The linearized equation may be written as follows

$$\frac{\mathrm{d}}{\mathrm{d}t} e_i^{(n)} = \sum_j (\tilde{\Omega}_{ij}^{(n)} + \hat{\Omega}_{ij}^{(n)}) e_j^{(n)} \tag{39}$$

Since Equation (39) has solutions of the form $e_i^{(n)}(t) = \hat{e}_i^{(n)} \exp(\sigma_l^{(n)} \cdot t)$, the one-dimensional boundary layer solution is considered to be unstable, if at least one real part of the complex eigenvalues $\sigma_l^{(n)} = \sigma_{lR}^{(n)} + \mathrm{i} \cdot \sigma_{lI}^{(n)}$ of the matrix $(\tilde{\Omega}_{i,j}^{(n)} + \hat{\Omega}_{i,j}^{(n)})$ is positive.

For fixed external parameters $(z_I - z_P)/z_P$, $\ln(z_p/z_0)$, Ro, Ro* and Ri, the eigenvalues $\sigma_l^{(n)}$ have been computed for many combinations of the horizontal wavenumber k_y and the orientation angle ϵ. This has been done for $(z_I - z_P)/z_P = 23$, $\ln(z_P/z_0) = 11$, $\mathrm{Ro}^{-1} = 7.2 \cdot 10^{-3}$, $\mathrm{Ro}^{*-1} = 0$, Ri = 0 (a), Ri = −0.05 (b), Ri = − 0.10 (c) and Ri = −0.15 (d).

For neutral stratification (Ri = 0), the results are shown in Figure 2a. Amplification rates denoted by solid lines are in units of $|\underline{v}_g|/(z_I - z_P) \cdot 10^{-2}$, the radial coordinate is the inverse aspect ratio and the angular coordinate is the orientation angle which is measured counterclockwise from the direction of the geostrophic flow to the axis of the rolls. The isoline $\sigma_{lR}^{(n)} = 0$ fixes the areal limits in the $(k_y/(2\pi), \epsilon)$-plane in which the inflection point instability can occur. The maximum amplification occurs with aspect ratio L/H = 2.4 and angle $\epsilon = -10°$. The phase speed of the most unstable perturbation is c = 0.219 which equals approximately the value of $\bar{v}$ at the position of the inflection point.

Figures 2b–2d show amplification rates as functions of inverse aspect ratio and orientation angle for unstable stratification.

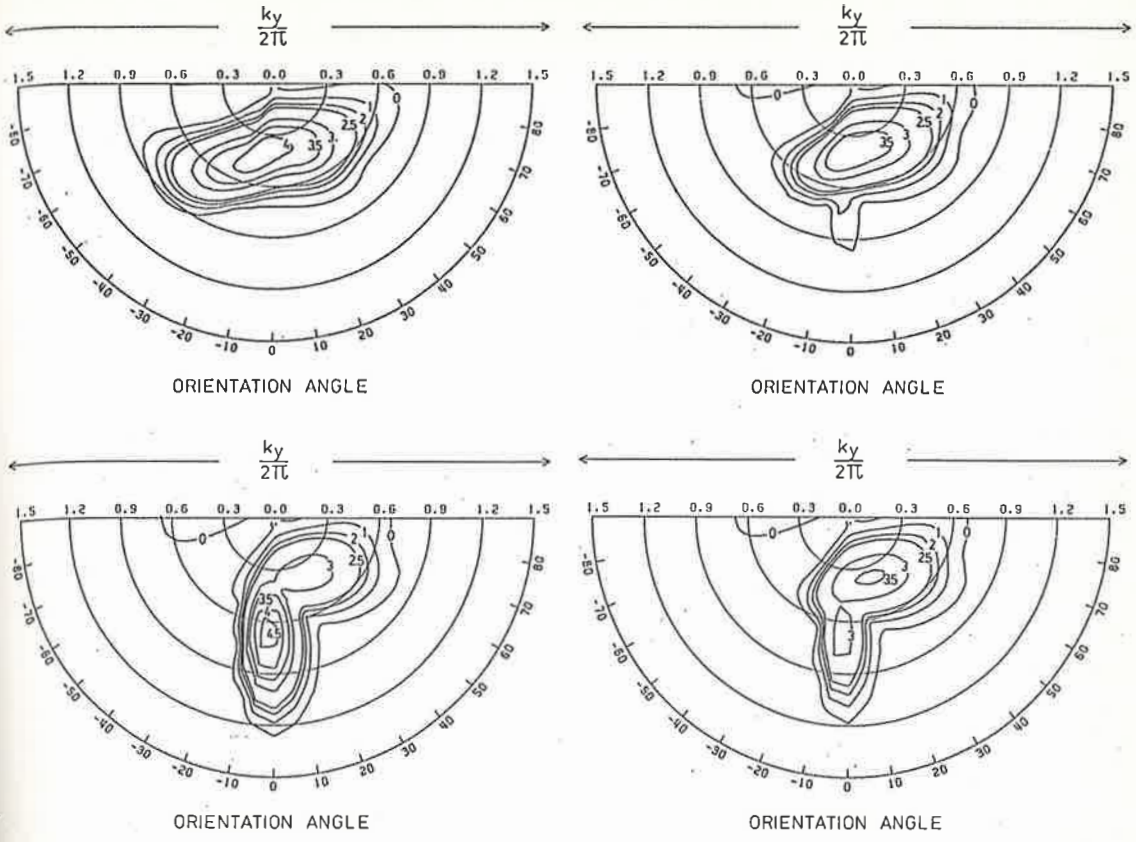

- **Figure 2a** Non-dimensional growth rates $\sigma_{IR}^{(n)} \cdot 10^2$ of unstable perturbations as functions of the inverse aspect ratio $H/L = k_y/(2\pi)$ (radial coordinate) and orientation angle ϵ (angular coordinate) for $(z_I - z_P)/z_P = 23$, $\ln(z_P/z_0) = 11$, $Ro^{-1} = 7.2 \cdot 10^{-3}$, $Ro^{*-1} = 0$ and $Ri = 0$.
- **Figure 2b** Same as Figure 2a, except $Ri = -0.05$.
- **Figure 2c** Same as Figure 2a, except $Ri = -0.10$.
- **Figure 2d** Same as Figure 2a, except $Ri = -0.15$.

For $Ri = -0.05$ the maximum growth rate position shifts to a roll orientation of $\epsilon = 0°$. The aspect ratio remains fairly constant at $L/H = 2.4$. The phase speed of the most unstable perturbation is $c = 0.052$. Moreover, an additional mode emerges at $\epsilon = 0°$ and $L/H = 1.48$ which propagates with $c = 0.146$. It appears that the latter is caused by thermal instability modified by shear flow and the former is attributed essentially to dynamic instability associated with shear flow having a point of inflection in its velocity profile. The unstable mode of thermal type seems to move at the velocity of the vertical mean of $\bar{v}$ and its amplification rate is about 0.25 times the amplification rate of the dynamic mode.

For $Ri = -0.10$ two distinct unstable regions exist in the $(k_y/(2\pi), \epsilon)$-plane. The maximum growth rate position of the dynamical mode is now located at $\epsilon = 18°$ and $L/H = 2.8$; the maximum amplification rate of the thermal mode occurs with $\epsilon = -2°$ and $L/H = 1.48$. The growth rates of the two modes are of about equal magnitude at this Richardson number.

A comparison of Figure 2c and 2d shows that the growth rates of the thermal mode increase with increasing static instability. For $Ri = -0.15$ the maximum growth rate is about 1.5 times that of the

dynamic mode; also the area in the $(k_y/(2\pi), \epsilon)$-plane, in which thermal instability can occur, is enlarged with increasing unstable stratification.

In contrast, enhanced turbulent diffusivities tend to stabilize the dynamic mode as the Richardson number decreases. In addition, the aspect ratio L/H and the angle ϵ, at which the maximum instability of the dynamic mode occurs, increase with increasing unstable stratification.

3.3 Results of non-linear integrations

3.3.1 Variation of mean flow kinetic energy and roll kinetic energy with time

A number of time integrations of Equation (38) and of Equations (27)–(29) was made using the parameters given in Section 3.1. The angle of the domain relative to the direction of the geostrophic wind was $\epsilon = -10°$ (Ri = 0), $\epsilon = 0°$ (Ri = −0.05), and $\epsilon = -2°$ (Ri = −0.10 and Ri = −0.15). The fundamental horizontal wavelength was L/H = 9.66 (Ri = 0), L/H = 5.91 (Ri = −0.05, Ri = −0.10, Ri = −0.10, Ri = −0.15), respectively.

Figure 3a shows the variation of the mean flow kinetic energy E and of the one-dimensional roll kinetic energy spectrum $E_{r,\,ky}$ with time for Ri = 0. E ist plotted as a departure from E_0 the value of the mean flow kinetic energy of the unperturbed initial state and the one-dimensional roll kinetic energy spectrum is normalized by means of the square of the geostrophic wind. Times on the abscissa are given in fractions of the dimensionless inertial period $P_T = 2\pi/f_1 \, |\underline{v}_g|/(z_I - z_P) = 2\pi \cdot Ro = 872$.

The initial development of the roll kinetic energy spectrum consists of a short exponential growth phase, followed by a noisy time series consisting of variations on a time scale determined by the large eddies. In the new statistically steady state the time averaged kinetic energy contained in the Fourier-components with the wavenumbers $k_y = 1.30$, $k_y = 1.95$ and $k_y = 2.6$ is nearly equal. The contribution of these wavenumbers to the total roll kinetic energy amounts to about 70%. Due to the normalization of $E_{r,\,ky}$ with $|\underline{v}_g|^2$ it is apparent that the perturbation energy is only a small fraction of the total energy.

The oscillations in the mean flow kinetic energy E were a small percentage of E and represented very small variations of the mean flow velocities. The mean flow kinetic energy exhibits an initial decrease due to the drain of energy from the developing perturbations and then shows a damped oscillation with period approximately P_T. The long time-scale oscillation is clearly an inertial oscillation exited initially by the amplifying perturbations.

In the unstable cases (Figures 3b–3d) a time from 1 to 2 periods P_T was usually required for the perturbations to adjust from the initial state to a new statistically steady state. In contrast with the neutral case, the time series of the roll kinetic energy spectrum exhibits a less erratic behaviour. As shown in Figures 3b–3d, a more or less unharmonic periodic solution is achieved with periods in the range between $1/20$–$1/3\ P_T$. At Ri = −0.05 61% of the total roll kinetic energy is included in the Fourier-components with the horizontal wavenumber $k_y = 1.062$. At Ri = −0.10 and Ri = −0.15 the maximum of the roll kinetic energy spectrum occurs at the horizontal wavenumber $k_y = 3.187$; the contribution of this wavenumber to the total roll kinetic energy amounts to 43% and 58%, respectively. The time history of the mean flow kinetic energy is again well represented by a damped inertial oscillation where amplitude and decay rate of this oscillation increase with increasing static instability.

3.3.2 Spectral energetics

In this section we consider in detail the mechanisms by which the rolls obtain energy and investigate how the dynamics of such rolls depend upon the relative importance of shear and buoyant forces.

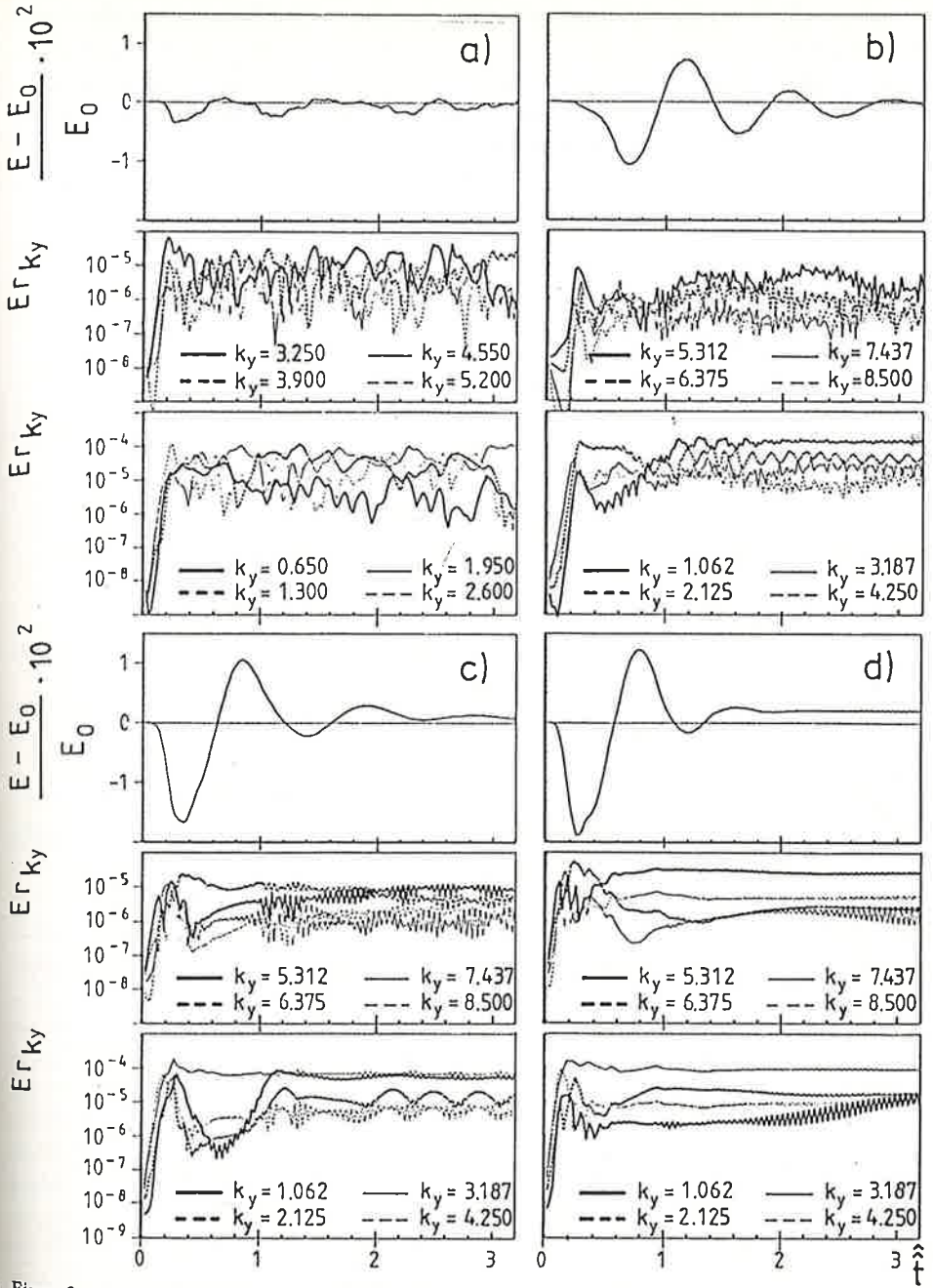

- **Figure 3a** Time series of mean flow kinetic energy E and of the non-dimensional one-dimensional roll kinetic energy spectrum $E_{r,\,k_Y}$ for the case $(z_I - z_P)/z_P = 23$, $\ln(z_P/z_0) = 11$, $Ro^{-1} = 7.2 \cdot 10^{-3}$, $Ro^{*-1} = 0$ and $Ri = 0$ and $\epsilon = -10°$. E is plotted as a departure from E_0, the value of the mean flow kinetic energy of the unperturbed initial state. Times on the abscissa are given in fractions of the dimensionless inertial period $P_T = 2\pi/f_1 \cdot |\underline{v}_g|/(z_I - z_P) = 2\pi \cdot Ro = 872$.
- **Figure 3b** Same as Figure 3a, except $Ri = -0.05$ and $\epsilon = 0°$.
- **Figure 3c** Same as Figure 3a, except $Ri = -0.10$ and $\epsilon = -2°$.
- **Figure 3d** Same as Figure 3a, except $Ri = -0.15$ and $\epsilon = -2°$.

Physical instability mechanisms leading to the occurence of rolls are known. Roll vortices can be generated by buoyancy or by shear or a combination of the two. In order to identify the instability mechanisms responsible for the generation of rolls we examine the spectral roll kinetic energy budget. In this way we quantify the various energy exchange processes in the production and maintenance of rolls and also trace in which way energy is interchanged between convective elements of different sizes.

It is convenient to split the kinetic energy of the secondary motion in two parts. The first is the roll kinetic energy E_r which is the energy of the wind components in the y-z plane and the second is the longitudinal energy E_l which is the energy of the along roll wind component. Hence, the volume average of E_r and E_l are defined as

$$\langle E_r \rangle = \frac{1}{LH} \int_0^H \int_0^L \tfrac{1}{2}(v'^2 + w'^2)\, dz\, dy = \sum_{ky=1}^{P} E_{r,ky}$$

$$\langle E_l \rangle = \frac{1}{LH} \int_0^H \int_0^L \tfrac{1}{2} u'^2\, dz\, dy = \sum_{ky=1}^{P} E_{l,ky}$$

where $E_{r,ky}$ and $E_{l,ky}$ are the one-dimensional spectra of roll kinetic energy and of the longitudinal energy, respectively. The spectral energy budget equations for two-dimensional flows can be derived from Equation (38) and can be written as:

$$\frac{\partial E_{r,ky}}{\partial t} = -\langle v'w' \frac{d\bar{v}}{dz} \rangle_{ky} + g/T_0 \langle w'T' \rangle_{ky} - f_1 \langle u'v' \rangle_{ky} + T_{r,ky} + D_{r,ky} \tag{40a}$$

$$\frac{\partial E_{l,ky}}{\partial t} = -\langle u'w' \frac{d\bar{u}}{dz} \rangle_{ky} + f_1 \langle u'v' \rangle_{ky} + T_{l,ky} + D_{l,ky} \tag{40b}$$

The various terms on the right hand side of these equations have the same significance here as they have in the physical space versions except that they relate only to production interchange and abstraction as these processes affect a single wavenumber component in the structure.

The first term on the right hand side of Equation (40a) and (40b) represents the production of roll energy and longitudinal energy from the kinetic energy of the mean cross roll and along roll wind components, respectively. The shear production arises from the interaction of the Reynolds stresses and the mean wind components. The second term in Equation (40a) is the production of roll energy by buoyancy which describes the flow of energy from the reservoir of potential energy to roll kinetic enery by means of a positive heat flux. The term $f_1 \langle u'v' \rangle_{ky}$ represents the conversion of roll kinetic energy between the longitudinal and the lateral wind components through the action of the Coriolis acceleration. $T_{r,ky}$ and $T_{l,ky}$ stand for the spectral transport or the divergence of the transfer of energy between different scales of motion. It is this transfer, non-linear in nature, which is responsible for the transmission of energy through the spectrum. Since these terms contribute nothing to the total energy (the non-linear transfer terms sum up to zero over all k_y), they only must serve to redistribute energy among wavenumbers. The last terms in Equation (40a) and (40b) represent the secondary dissipation, i.e the energy loss due to the interaction of the rolls with the three-dimensional turbulence field. In equilibrium, the exchange of roll-scale energy with smaller scale turbulence, i.e. the secondary dissipation, must equal the production, transfer and redistribution terms.

In summary, the metamorphosis of roll-scale turbulence comprehends four phenomena: production, non-linear transfer, interchange and dissipation. Figure 4 schematically illustrates these energy exchange processes which take place in finite amplitude rolls. In the picture the term $\langle p' \partial u'/\partial x \rangle$ represents an additional mechanism interchanging energy from the u' to the v' and w' components. The pressure-gradient transfer term neither creates nor destroys energy, but it does act to transfer it among the lon-

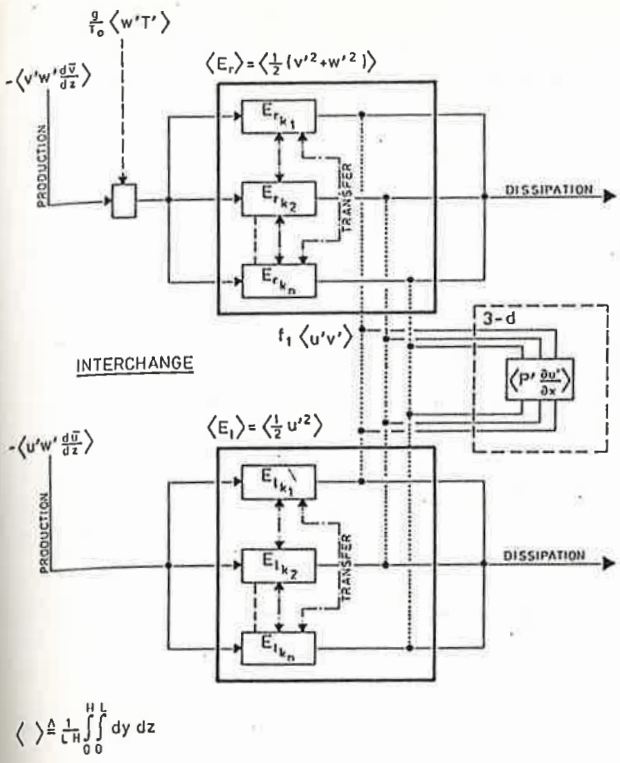

- **Figure 4**
  Schematic diagram of the longitudinal energy and of the roll kinetic energy budget.

gitudinal and lateral components. The effect of this correlation is to make the velocity field less anisotropic since the transfer of energy is from the higher intensity to the lower intensity components. However, this equalisation is only possible in models with three-dimensional dynamics since the two-dimensional approximation requires $\partial u'/\partial x = 0$.

The non-dimensional roll kinetic energy budget terms for neutral and unstable conditions are presented in Figures 5a–5d. Shown are in semi-logarithmic plots spectra of shear production P_{ky} (solid), of buoyancy production A_{ky} (dashed), of Coriolis transfer C_{ky} (dotted), of non-linear transfer T_{ky} (dash-dotted) and of dissipation D_{ky} (thick solid) as functions of the wavenumber k_y. The spectra are obtained by computing these quantities at each time step, then averaging these spectra over a long time period. For the results presented below, the integration was continued up to $t \cong 4.5 P_T$ and the time average was taken over the last inertial period P_T.

In the neutral case (Figure 5a) energy is fed from shear into roll kinetic energy in the wavenumber range between $k_y = 0.65$ and $k_y = 3.25$. Energy loss due to secondary dissipation also takes place mainly in this range. Inertia forces, or vortex stretching due to the fluctuating velocity gradient, mainly serve to transfer the rest of the energy gain from lower to higher wavenumbers. The Fourier-components in the higher wavenumber range between $k_y = 3.9$ and $k_y = 5.2$ receive their energy mainly due to non-linear transfer. In equilibrium this energy is released to the reservoir of the turbulent kinetic energy and the lateral mean flow energy, respectively. The energy gain (loss), due to the Coriolis forces is much smaller than due to the dominant processes in the energy budget so that the Coriolis transfer can be excluded from the considerations. This is in agreement with observational results obtained by BRÜMMER (1985) who also proved the Coriolis terms to be insignificant in transferring energy from the longitudinal to the lateral velocity component.

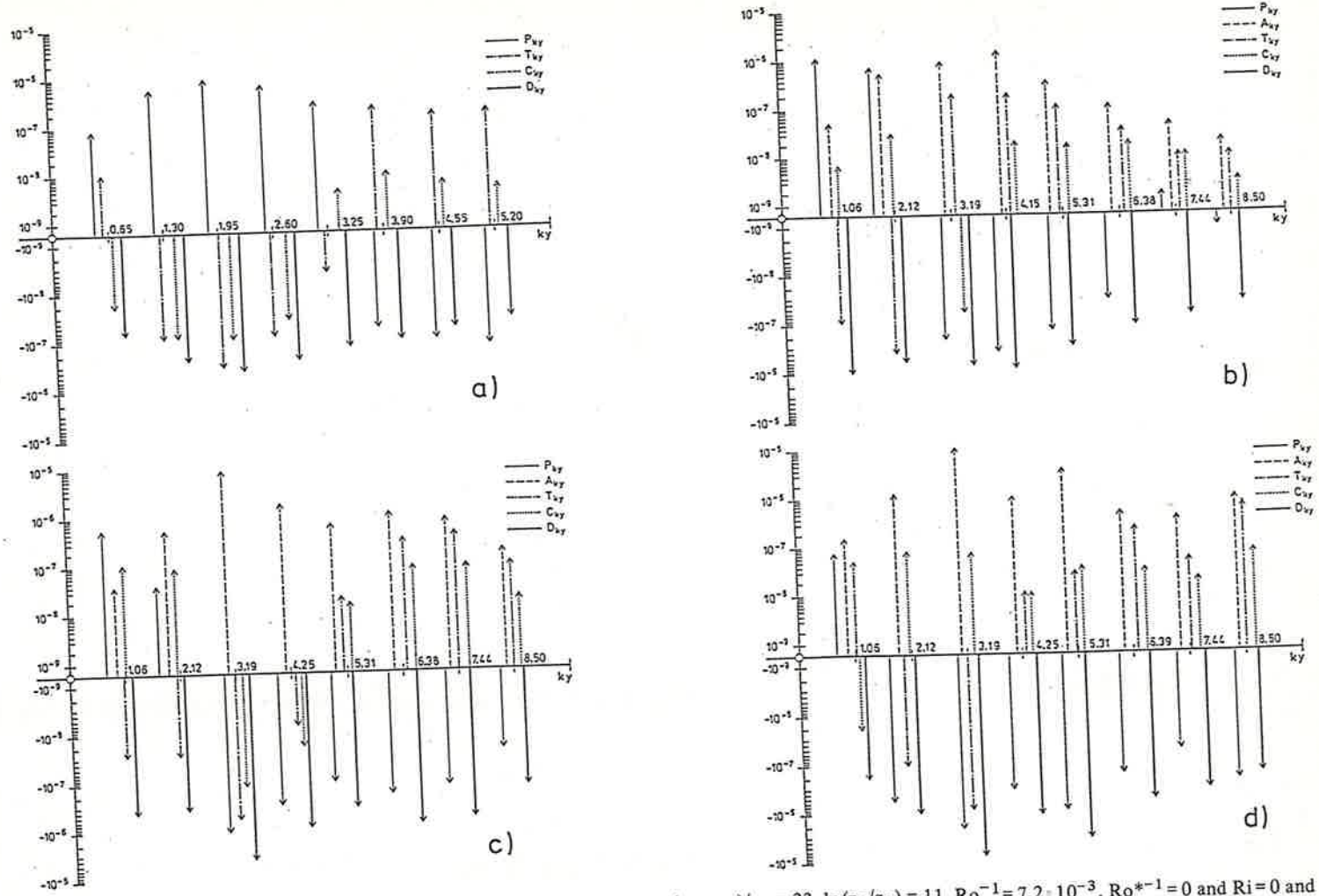

- **Figure 5a** Non-dimensional spectral roll energy budget terms for the case $(z_I - z_P)/z_P = 23$, $\ln(z_P/z_0) = 11$, $Ro^{-1} = 7.2 \cdot 10^{-3}$, $Ro^{*-1} = 0$ and $Ri = 0$ and $\epsilon = -10°$. Shown are the spectra of shear production P_{ky} (solid), of buoyancy production A_{ky} (dashed), of Coriolis transfer C_{ky} (dotted), of non-linear transfer T_{ky} (dash-dotted) and of dissipation D_{ky} (thick solid) as functions of the non-dimensional wavenumber k_y.
- **Figure 5b** Same as Figure 5a, except $Ri = -0.05$ and $\epsilon = 0°$.
- **Figure 5c** Same as Figure 5a, except $Ri = -0.10$ and $\epsilon = -2°$.
- **Figure 5d** Same as Figure 5a, except $Ri = -0.15$ and $\epsilon = -2°$.

In the unstable cases (Figures 5b–5d) energy from the buoyancy forces feeds into most of the parts of the wavenumber space. The maximum of the buoyancy production spectrum occurs at $k_y = 4.250$ (Ri = −0.05) and shifts to smaller wavenumbers with an increasing maximum of spectral density with increasing instability. It turns out that roll kinetic energy is produced mainly by release of potential energy contained in the unstable stratified fluid layer through upward heat transport and shear production, though significant, is not dominant. The shear production of the roll motions is confined to the lower wavenumber range and the ratio between the maxima of buoyant and shear production gives values between 1 (Ri = −0.05), 20 (Ri = −0.10) and 100 (Ri = −0.15). In addition, the non-linear transfer spectrum is negative at low wavenumbers and positive at high numbers, i.e. it tends to transform low wavenumber energy to high wavenumbers. Finally, since the vertical momentum flux is against the shear of the basic lateral flow a transformation of kinetic energy of the perturbations to that of the basic flow occurs, resulting in negative values of the shear production spectrum at intermediate and high wavenumbers. It should be emphasized that the wavelengths of the modes receiving the most buoyant and shear energy roughly correspond to those predicted from the perturbation theory. Perhaps this could be important for modellers working with low-order spectral models.

Summarizing the above discussion the rolls at Ri = 0 were driven by the mean wind shear while those at Ri = −0.10 and Ri = −0.15 seem to have been thermally driven since the buoyancy term significantly exceeds the shear production term. At Ri = −0.05 the vortices were generated by a combination of the inflection point and the thermal instability since the energy supplied to the rolls by these two mechanisms is nearly equal in magnitude.

3.3.3 Mean profiles

In this section we present dimensionless vertical profiles of mean velocity ($\bar{u}$, $\bar{v}$) and temperature $\bar{T}$, dimensionless roll scale variance profiles of longitudinal momentum u', of lateral momentum v' and of vertical velocity w', non-dimensional profiles of roll scale temperature transports and non-dimensional shear stress profiles. The flow statistics were obtained by averaging results from realisations over a inertial period P_T starting 3.5 inertial periods from the initial perturbation.

Figures 6a–6d show the mean velocity and temperature profiles for Ri = 0 (a), Ri = −0.05 (b), Ri = −0.10 (c) and Ri = −0.15 (d). Solid lines are used to denote the initial profiles and broken lines to denote the profiles in the statistical equilibrium after roll vortices have been generated.

For all Richardson numbers the initial along-roll wind component $\bar{u}$ is characterized by a weak maximum in the upper part of the roll layer and the cross roll component $\bar{v}$ exhibits a tangent like profile with an inflection point at about z = 0.75. Initial profiles of temperature show gradients in the lower third of the atmospheric boundary layer with a well mixed layer above.

At Ri = 0 a comparison between initial profiles and equilibrium profiles after the rolls have generated show that the divergence of the longitudinal momentum transports associated with the rolls reduce the mean vertical gradients of $\bar{u}$-momentum. In addition, the action of the cross-roll momentum flux divergence reduces the wind difference above and below the inflection point to relieve the vorticity maximum in the $\bar{v}$-component.

In the unstable cases (Figures 6b–6d) the divergence of the longitudinal momentum flux also decreases $\bar{u}$-momentum in the upper part of the boundary layer and increases $\bar{u}$-momentum in the lower part. In contrast, the mean lateral momentum $\bar{v}$ seems to be enhanced in all levels since buoyancy generated roll kinetic energy is transfered to the reservoir of the lateral mean flow energy (see Section 3.3.2). Finally, temperature fluxes associated with the rolls lower the temperature difference between the top and the bottom of the Ekman layer. It should be mentioned that in Figures 6b–6d the non-dimensional temperature increases with height, which corresponds to a decrease in the dimensional temperature with

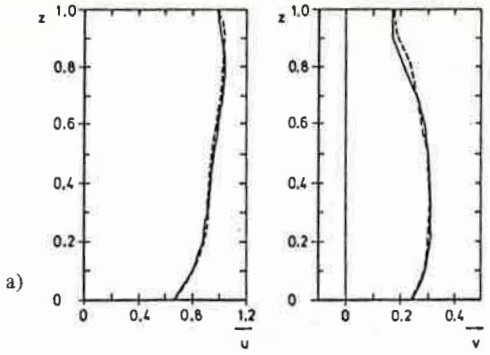

- **Figure 6a** Vertical profiles of non-dimensional mean velocity components longitudinal $\bar{u}$ and lateral $\bar{v}$ to the rolls for the case $(z_I - z_P)/z_P = 23$, $\ln(z_P/z_0) = 11$, $Ro^{-1} = 7.2 \cdot 10^{-3}$, $Ro^{*-1} = 0$ and $Ri = 0$ and $\epsilon = -10°$. Solid lines are used to denote the initial profiles and broken lines to denote the profiles in the statistical equilibrium after roll vortices have been generated.

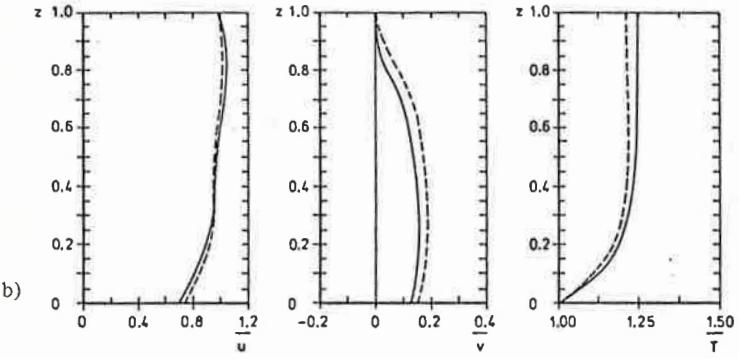

- **Figure 6b**
  Same as Figure 6a, except $Ri = -0.05$ and $\epsilon = 0°$. Additionally, vertical profiles of non-dimensional mean temperature $\bar{T}$ are presented.

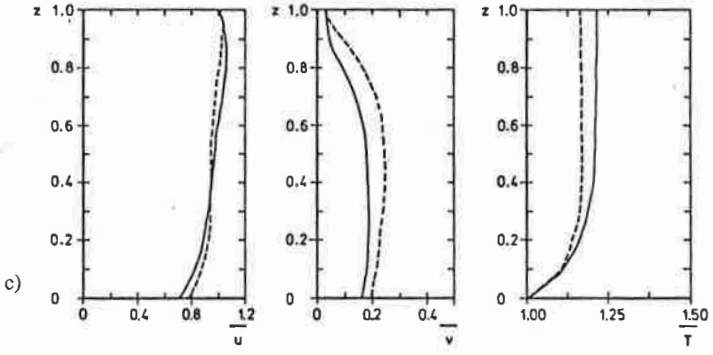

- **Figure 6c**
  Same as Figure 6b, except $Ri = -0.10$ and $\epsilon = -2°$.

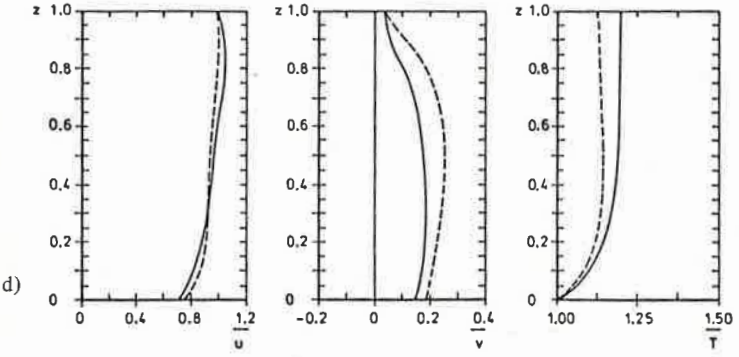

- **Figure 6d**
  Same as Figure 6b, except $Ri = -0.15$ and $\epsilon = -2°$.

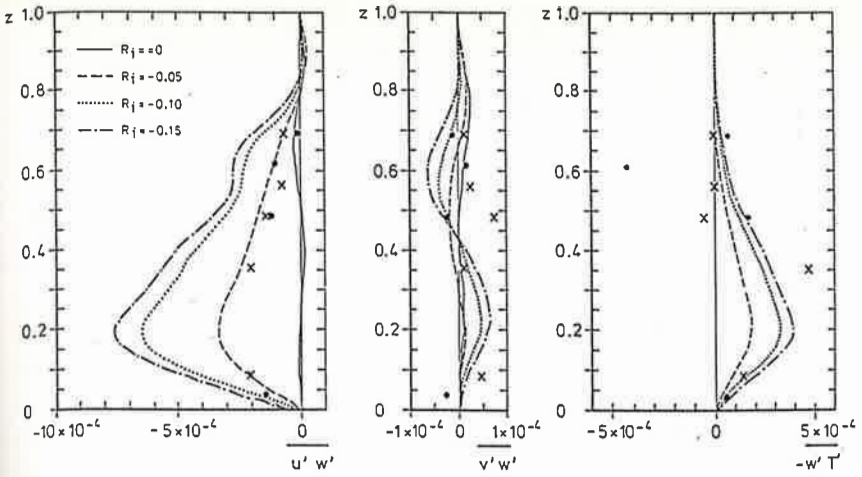

Figure 7 Calculated and measured non-dimensional mean vertical roll-scale transports of temperature, of along-roll and cross-roll momentum as functions of dimensionless height for the cases $(z_I - z_P)/z_P = 23$, $\ln(z_P/z_0) = 11$, $Ro^{-1} = 7.2 \cdot 10^{-3}$, $Ro^{*-1} = 0$, $Ri = 0$ (solid), $Ri = -0.05$ (dashed), $Ri = -0.10$ (dotted) and $Ri = -0.15$ (dash-dotted). Data are marked with dots and crosses and refer to aircraft measurements from FALCON and HERCULES on September 20, 1981 (after BRÜMMER, 1985). The normalization factors are $|\underline{v}_g|^2 = 400 \cdot m^2 s^{-2}$ and $|\underline{v}_g| \cdot (\overline{T}(z_P) - \overline{T}(z_0)) = -20\ ms^{-1}K$, respectively.

height (which would be a more "conventional" graph), since the latter is made dimensionless by the temperature difference between the top and the bottom of the Prandtl-layer $(\overline{T}(z_P) - \overline{T}(z_0))$ which is negative in an unstable boundary layer.

Roll-scale vertical fluxes of temperature T', u'- and v'-momentum are presented in Figure 7 for Ri = 0 (solid), Ri = -0.05 (dashed), Ri = -0.10 (dotted) and Ri = -0.15 (dash-dotted). Measured values shown by data points in Figure 7 are from aircraft observations of BRÜMMER et al. (1985) performed on the 20th September 1981 during the KonTur experiment. These are normalized using $|\underline{v}_g|^2 = 400\,m^2s^{-2}$ and $|\underline{v}_g|(\overline{T}(z_P) - \overline{T}(z_0)) = -20\,ms^{-1}K$ as scale factors, respectively.

Cloud streets observed during this day seem to have been thermally driven. BRÜMMER (1985) calculated several of the energy production terms and shows that the buoyancy term was large on this day and shear production was insignificant.

The measured along-roll momentum flux has its maximum around z = 0.2 and decreases rapidly with height to values near zero at the top of the boundary layer. The cross roll momentum flux was generally smaller and scattered around zero. The slightly unstable stratification near the sea surface is reflected in positive temperature fluxes in the lower part of the boundary layer. The temperature flux decreases with height and becomes negative at higher levels due to the entrainment of warmer air above the inversion.

The profiles calculated for unstable conditions compare qualitatively well with the observational data. The rolls transport along-roll momentum downward, temperature upward and cross-roll momentum upward in the lower part of the convection layer and downward in the upper part. However, for the Richardson number Ri = -0.10, which corresponds roughly to the observations, the model seems to overestimate the along-roll momentum flux. In addition, the calculated temperature flux is positive in the whole layer and designed to give zero flux at z = 1. The actual heat flux must be negative at z = 1 due to downward entrainment of warm stable air into the convective region. However, this mechanism and the resulting tendency for the inversion base to increase with time could not modelled here.

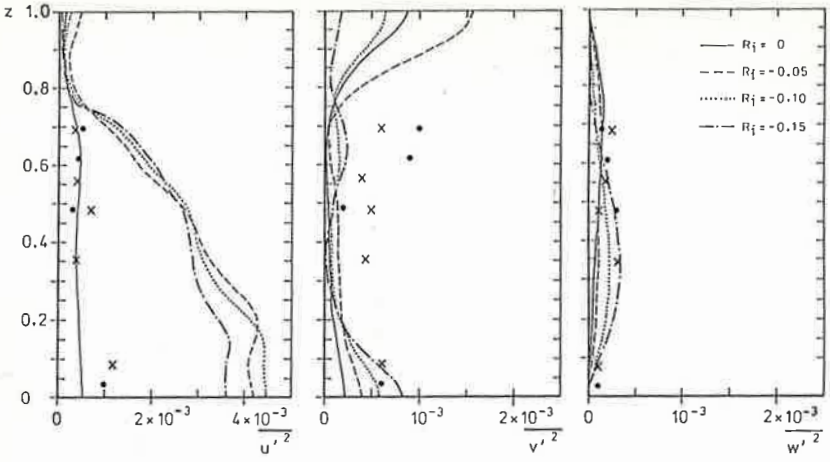

- **Figure 8**
  Calculated and measured profiles of non-dimensional roll-scale variances of along-roll u′, cross-roll v′ and vertical wind component w′ (other features as in Figure 7).

Calculated and measured profiles of the roll-scale horizontal and vertical velocity intensities are shown in Figure 8 (normalization factors as in Figure 7).

For Ri = 0 the roll-scale w′-variance appears to have a broad maximum in the upper part of the roll layer, not far away from the inflection point in the mean lateral wind component, where the largest shear is present. The roll-scale v′-variance has two maxima, at z = 0 and z = 1, as expected for a roll circulation. The ratio between the maximum variances of v′ and w′ is about 6:1. The intensities of the longitudinal u′-variance and the v′-variance are of the same order.

In the unstable cases the maximum of the vertical velocity variance occurs at z = 0.3. Form and maximum value of $\overline{w'^2}$ are very close to that seen in the KonTur observations. The roll-scale u′-variance has a maximum at z = 0 and decreases with height.

The most striking feature in Figure 8 is the enormous peak in the longitudinal energy as the Richardson number becomes negative. The calculated u′-variance in three times larger than the observed longitudinal energy intensity while the predicted values of v′-variance are the right order of magnitude, but systematically to small especially in the upper part of the boundary layer. The model predicts a ratio of $(u'^2)_{max}$ to $(v'^2)_{max}$ between 4:1 and 10:1, while observation indicates that $(u'^2)_{max}$ and $(v'^2)_{max}$ are of the same order.

The too large u′ seems common (if not universal) in previous two-dimensional roll theories (e.g. that of BROWN, 1970 or that of MASON and SYKES, 1982). Hence, the apparent discrepancy between results obtained from the model and observations highlights the inability of two-dimensional models to correctly describe the transport of along-roll perturbation into the cross-roll directions. The $(\overline{u'^2})$-profile is determined by the roll motion producing a vertical interchange of $\bar{u}$. Since the rolls are nearly aligned in the x-direction large deviations can be produced in the longitudinal component by the two-dimensional circulations sweeping fast moving fluid from outside the surface layer downwards. As a consequence of the two-dimensional approximation the longitudinal component is virtually decoupled from the dynamics of the other components resulting in an enhanced maximum in this component. Therefore, the apparent deficiency in the longitudinal energy intensity seems to be caused by the lack of efficient mechanisms transferring energy from the u′-component to the v′- and w′-components.

Three-dimensional effects would probably reduce the roll-scale variance ratio $(\overline{u'^2/v'^2})$ because as a result of the pressure-velocity-gradient correlation $\overline{p'\partial u'/\partial x}$ coupling of u′-momentum to v′- and w′-momentum is stronger than two-dimensional models suggest. As pointed out in Section 3.3.2 the effect of this correlation is to produce a equipartition of roll kinetic energy since the transfer of energy, via pressure forces, is from high-intensity to the lower-intensity component.

This assumption is supported by BECKERs (1987) three-dimensional boundary layer model which produces a considerably more realistic ratio of roll-scale u′- and v′-variance.

3.3.4 Secondary flow structure

Figures 9–12 illustrate typical realisations of the secondary flow pattern for fully developed rolls for integrations with different values of the Richardson number. Plotted are the isolines of the streamfunction ψ (a), of the vertical velocity w′ (b), of the longitudinal velocity perturbation u′ (c), and of the temperature perturbation T′ (d) in y-z cross sections through the vortex rolls. Streamfunction, velocity and temperature perturbations were normalized by using the maxima of these quantities occuring in the domain.

In Figure 9a three counterrotating vortex pairs are to be seen. The slope of the perturbations with height, indicated most clearly by the $\psi = 0$ lines, is characteristic of perturbations which are drawing energy from the mean lateral flow. These structures are not steady in form or highly regular though rolls propagating down the positive y-axis are the dominant feature. The phase speed of the vortices corresponds roughly to the velocity of the mean lateral wind component at the height of the inflection point. The centers of the cells and the maximum amplitudes of w′ and u′ occur at $z = 0.7$ which corresponds roughly to the height of the inflection point in the mean lateral wind profile. Dimensionless maximum values of w′ and u′ are 0.025 and 0.048, respectively (normalization factor is $|\underline{v}_g|$). The aspect ratio of the rolls was determined by calculating horizontal distances between neighbouring updrafts at each time step, then averaging these quantities over an inertial period P_T. In the neutral case the time averaged aspect ratio is $\lambda = 2.7$ and the standard deviation is $\sigma = 0.86$.

Typical realisations of the secondary flow pattern for unstable conditions are presented in Figures 10–12. In these cases more vigorous eddies are produced. The flow is determined by three rolls propagating down the positive y-axis with a phase speed which corresponds roughly to the vertical mean of $\bar{v}$. Note that the centers of the cells and the maximum amplitudes of the vertical and the longitudinal velocity perturbations occur now (except for Ri = −0.05) significantly below the mid-level. The picture of the secondary flow pattern shown here is in qualitative agreement with model results obtained by MASON and SYKES (1982). Their modelling effort also produces roll vortices which resemble structures consistent with instability theories.

The magnitude of the roll motions varies from case to case. With Ri = −0.05, Ri = −0.10 and Ri = −0.15, the dimensionless peak vertical motions are 0.025, 0.030, and 0.037, respectively (normalization factor is $|\underline{v}_g|$). The non-dimensional peak amplitudes of the longitudinal velocity perturbations are $(u')_{max} = 0.143$ (Ri = −0.05), $(u')_{max} = 0.149$ (Ri = −0.10), $(u')_{max} = 0.141$ (Ri = −0.15). The temperature perturbations T′ are determined largely by the vertical advection of the mean temperature $\bar{T}$. Hence, large values of T′ were confined to the region below $z = 0.3$, the region of strong gradients in $\bar{T}$. The non-dimensional peak amplitudes are $(T')_{max} = 0.0598$ (Ri = −0.05), $(T')_{max} = 0.060$ (Ri = −0.10) and $(T')_{max} = 0.0566$ (Ri = −0.15) (normalization factor is $(\bar{T}(z_P) - \bar{T}(z_0))$).

The most remarkable feature is that the pattern of the vertical velocity field is in phase with the temperature perturbation field, i.e. maximum temperature perturbations coincide with the strongest upward motions and vice versa, indicating conversion between the potential energy and roll kinetic energy. In addition, the vertical velocity field shows a phase shift of roughly $\frac{1}{2}$ (L/H) with respect to the field of the longitudinal velocity component, forming a roll-scale downward momentum flux. It should be noted that in the average the slope of the rolls at the more unstable Richardson numbers (Ri = −0.10 and Ri = −0.15) is invers to that in the neutral case, implying that the rolls are returning energy to the mean lateral flow (this is indicated most clearly in the upper part of the boundary layer).

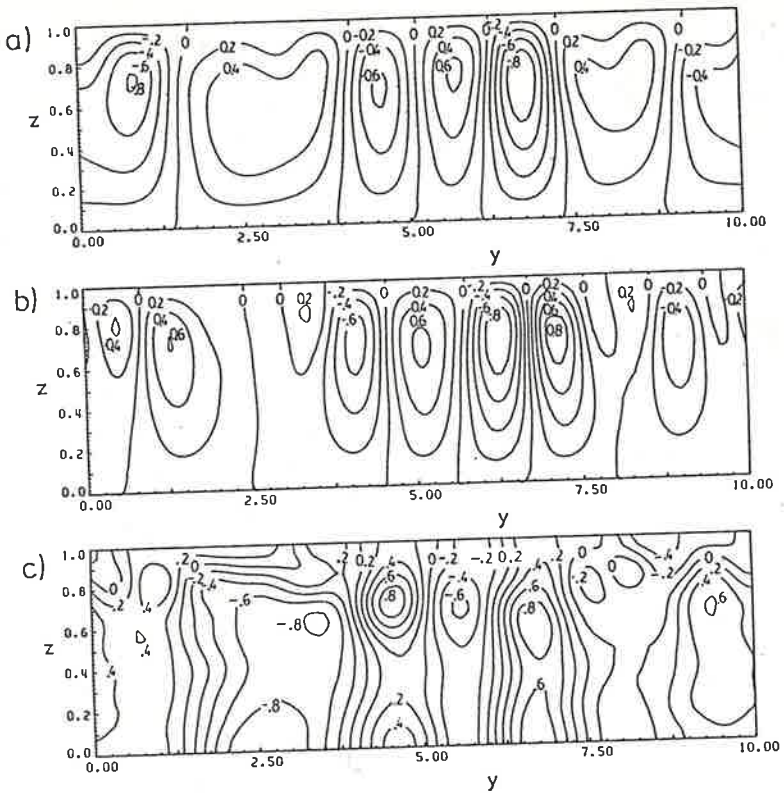

Figure 9 Typical realisation of the secondary flow pattern for the case $(z_I - z_P)/z_P = 23$, $\ln(z_P/z_0) = 11$, $Ro^{-1} = 7.2 \cdot 10^{-3}$, $Ro^{*-1} = 0$ and $Ri = 0$ and $\epsilon = -10°$. Plotted are contours of the streamfunction ψ (a), the along-roll u' (b) and the vertical velocity component w' (c) in y–z cross sections. Streamfunction and velocity perturbations were normalized by using the maxima of these quantities occurring in the domain.

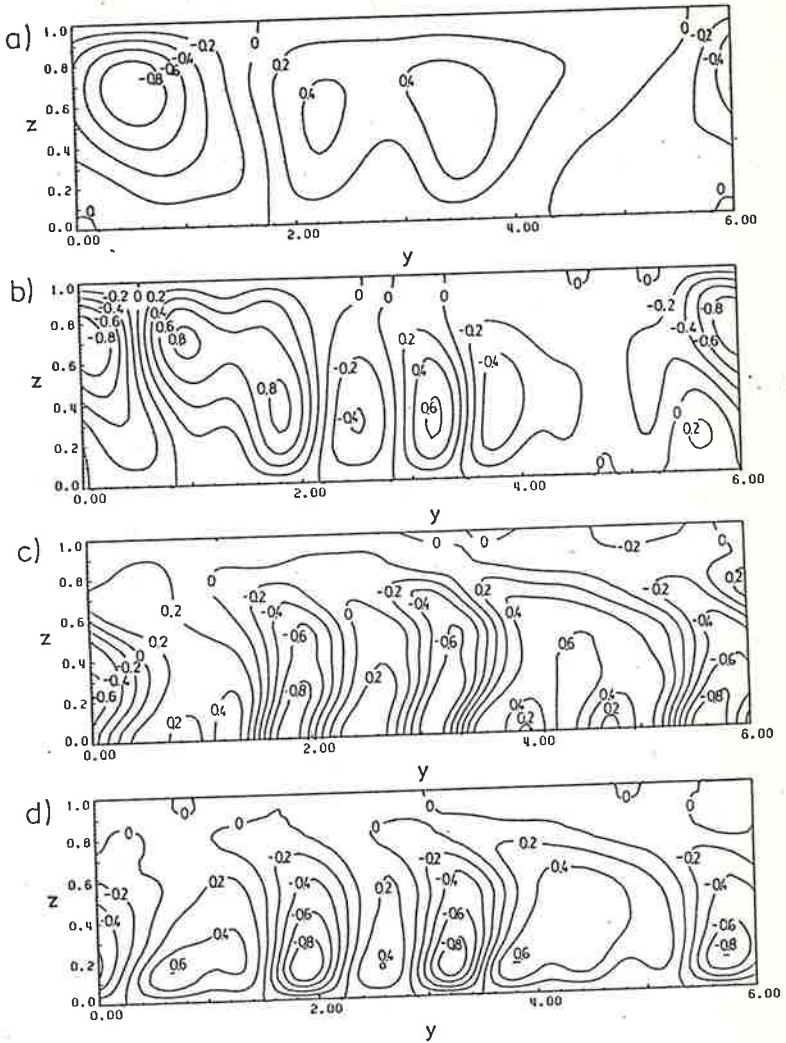

Figure 10 Same as Figure 9, except $Ri = -0.05$ and $\epsilon = 0°$. Additionally, contours of temperature perturbations T' (d) are shown.

The horizontal scale of the rolls is greater than the wavelength of the fastest growing linear mode but similar to atmospheric observations. Averaging horizontal distances between neighbouring updrafts yields

$\lambda = 2.9 \quad \sigma = 0.90 \quad Ri = -0.05$
$\lambda = 3.2 \quad \sigma = 0.97 \quad Ri = -0.10$
$\lambda = 2.5 \quad \sigma = 0.62 \quad Ri = -0.15$

For the Richardson number of Ri = −0.10, which corresponds roughly to the situation on the 20.9.81, the calculated aspect ratio is in reasonable agreement with the observational mean value of 2.9. The agreement is not only restricted to the mean value, but also concerns the variability of the aspect ratio. In the observations the distance between individual cloud lines varies between 1.3 and 5, while aspect ratios occuring in the model range from 1.5 to 6.

4 Summary and Conclusions

The properties of large scale roll motions in neutral and unstable atmospheric boundary layers have been investigated by means of a numerical spectral model. The roll vortices are assumed to be two-dimensional and they are modelled explicitly in a vertical plane of variable orientation with respect to the geostrophic flow.

First, a linear stability analysis has been performed for various Richardson numbers to confirm that the fundamental instability mechanisms leading to the occurence of rolls are the inflection point instability and shear organized buoyant convection. In addition, the stability calculations have shown that the most unstable perturbations exhibit maximum growth rates for orientations close to the direction of the geostrophic wind.

Second, finite amplitude integrations have illustrated a number of features worthy of note. It was found that the perturbations come to a non-linear equilibrium, producing a modified mean flow and a helical roll secondary roll circulation with a horizontal wavelength of about three times the convection layer depth. It was demonstrated that in the neutral case the eddies were driven by a shear flow instability. This contrasts with the study of a slightly unstable stratified boundary layer when Ri is less than −0.05. In this case more vigorous eddies are produced. Examination of the energetics shows that the rolls are essential buoyancy driven and shear production, though significant, was not dominant. In contrast to the roll motions, the component of the motion parallel to the rolls is the recipient of a large shear production.

When Ri = −0.10, conditions are typical of observations of roll vortices on the 20th September 1981 during the KonTur experiment. Comparison of the results obtained with the model and observations performed during this day exhibits possibilities and limitations of two-dimensional modelling. Whereas the predicted geometrical parameters of the flow, like orientation angle and band spacing, are within the limits to be observed the secondary flow statistics could only be qualitatively reproduced by the model. In particular, as pointed out in Section 3.3.3, the apparent deficiency in the longitudinal energy intensity seems to be a consequence of using a two-dimensional model where the longitudinal component is virtually decoupled from the dynamics of the cross-roll components.

Therefore, an extension towards a better representation of three-dimensionality would be desirable. In addition, it is planned to extend the model to allow the entrainment process at the top of the boundary layer to be modelled and to include water vapor and liquid water to examine some of the effects of moisture and clouds upon the roll motions.

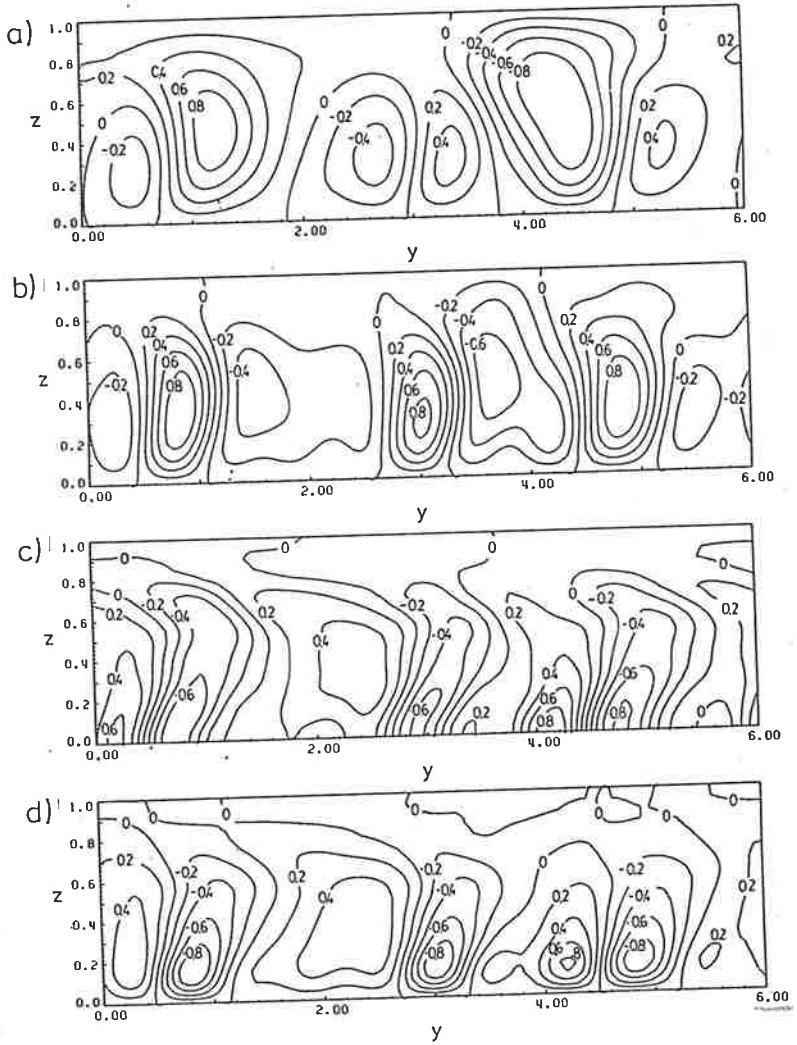

• **Figure 11** Same as Figure 10, except Ri = −0.10 and $\epsilon = -2°$.

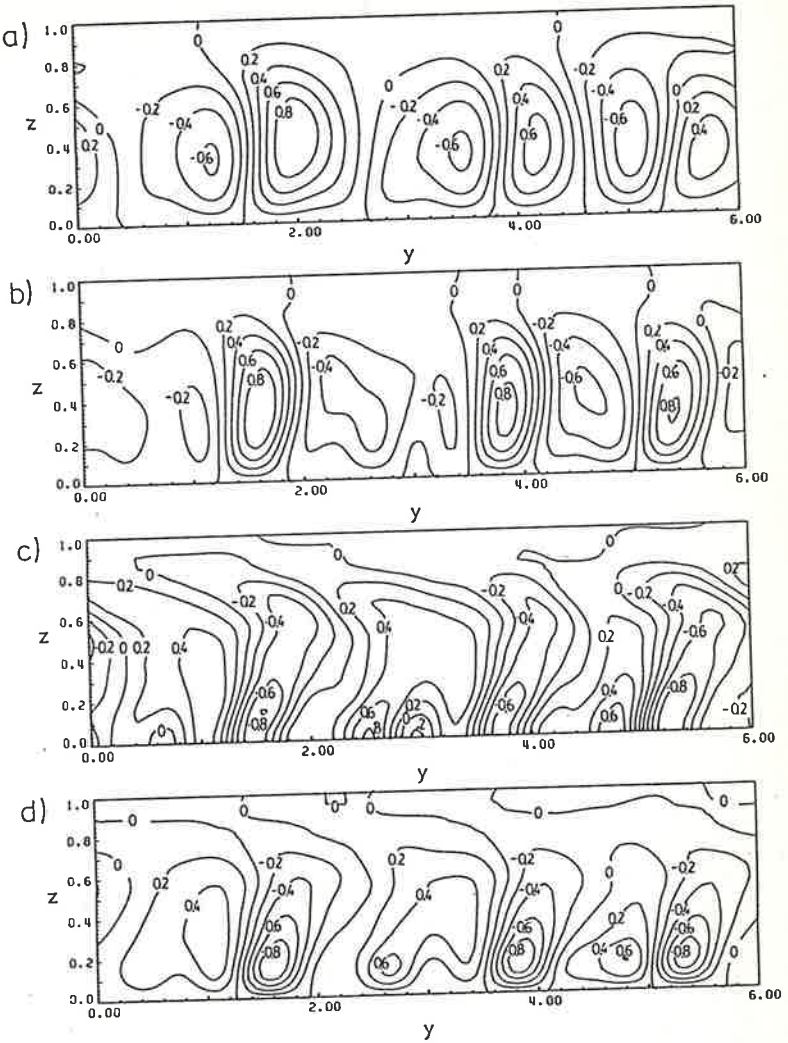

• **Figure 12** Same as Figure 10, except Ri = −0.15 and $\epsilon = -2°$.

Acknowledgements

The author whishes to thank Prof. Dr. H. HINZPETER for his useful comments and close inerest in this study.

References

ASAI, T. and I. NAKASUJI, 1973: On the stability of Ekman boundary layer flow with thermally unstable stratification. J. Meteor. Soc. Japan **51**, 29–41.

BECKER, P., 1987: Three-dimensional investigation of roll vortices: a case study. Beitr. Phys. Atmosph. **60**, 170–179

BROWN, R. A., 1970: A secondary flow model for the planetary boundary layer. J. Atmos. Sci. **27**, 742–757.

BROWN, R. A., 1972: On inflection point instability of a stratified Ekman boundary layer. J. Atmos. Sci. **29**, 850–859.

BRÜMMER, B., S. BAKAN and H. HINZPETER, 1985: KonTur observations of cloud streets and open cellular structures. Dynamics of Oceans and Atmospheres **9**, 281–296.

BRÜMMER, B., 1985: Structure, dynamics and energetics of boundary layer rolls from KonTur aircraft observations. Beitr. Phys. Atmosh. **58**, 237–254.

BUSINGER, J. A., J. C. Wyngaard, Y. IZUMI and e. F. BRADLEY, 1971: Flux relationship in atmospheric surface layer. J. Atmos. Sci. **28**, 181–189.

CHLOND, A., 1985: A study of roll vortices in the atmospheric boundary layer. Beitr. Phys. Atmosph. **58**, 17–30.

ETLING, D. and F. K. WIPPERMANN, 1975: On the instability of a PBL with Rossby number similarity, Part 1. Bound. Layer Meteorol. **9**, 341–360.

KÜTTNER, J. P., 1971: Cloud bands in the earth's atmosphere. Tellus **23**, 404–425.

LE MONE, M. A., 1973: The structure and dynamics of horizontal roll vortices in the planetary boundary layer. J. Atmos. Sci. **30**, 1077–1091.

LILLY, D. K., 1966: On the instability of Ekman boundary flow. J. Atmos. Sci. **23**, 481–491.

MACHENHAUER, B., 1979: The spectral method. In: Numerical methods used in atmospheric models, Vol 2, GARP PUBL. SER. No **17**, 124–277.

MASON, P. J. and R. I. SYKES, 1982: A two-dimensional numerical study of horizontal roll vortices in an inversion capped planetary boundary layer. Quart. J. R. Meteorol. Soc. **108**, 801–823.

SHIRER, H. N., 1980: Bifurcation and stability in a model of moist convection in a shearing enviroment. J. Atmos. Sci. **37**, 1586–1602.

WIPPERMANN, F. K., D. ETLING and H. J. KIRSTEIN, 1978: On the instability of a PBL with Rossby number similarity. Part 2. Bound. Layer Meteorol. **9**, 341–360